

# Investigations on the microstructure, mechanical, corrosion and wear properties of Mg–9Al–xGd (0, 0.5, 1, and 2 wt%) alloys

Karuna Ratnakaran Athul, Amirthalingam Srinivasan, and Uma Thanu Subramonia Pillai<sup>a)</sup>  
*Materials Science and Technology Division, National Institute for Interdisciplinary Science and Technology (NIIST), Council of Scientific & Industrial Research, Thiruvananthapuram 695019, India*

(Received 14 May 2017; accepted 8 August 2017)

Magnesium alloys with the lowest structural density exhibit unique applications in the automotive and aerospace fields. Rare earth addition is a promising method to enhance the mechanical properties of the Mg alloys. In the present study, the magnesium–aluminium (Mg–9Al) alloy containing varying wt% of gadolinium (Gd) is synthesized using the casting technique. The microstructure, mechanical, corrosion, and wear properties of the developed Mg–9Al–xGd alloy are evaluated and compared to the base Mg–9Al alloy. Microstructural investigation shows significant grain refinement and the presence of Al<sub>2</sub>Gd in addition to β-Mg<sub>17</sub>Al<sub>12</sub> in the Gd-added alloys. Under tensile loads, the developed Mg–9Al–2Gd alloy exhibits enhancements in ultimate and yield strengths. The corrosion resistance of the alloys is found to increase with increasing Gd content and is optimal at 2 wt%. Considering the higher hardness and dispersity of the Al<sub>2</sub>Gd phase, Mg–9Al–2Gd has exhibited a higher wear resistance than that of the as-cast Mg–9Al alloy.

## I. INTRODUCTION

The strict requirements of the transportation industry aiming at “safer, efficient, and cleaner” vehicles have led to the interest in the area of light metal alloys. Magnesium alloys are emerging as the perfect candidate with the lowest density among structural materials (1.74 g/cm<sup>3</sup>), high specific strength, good castability, excellent damping capacity, fine machinability, and good recycling potential.<sup>1</sup> Mg–Al and Mg–Al–Zn alloys are the most common alloys used for casting due to a wide spectrum of advantageous properties. However, the application of magnesium alloys lags behind their competitors like aluminum and steel due to the inferior elevated-temperature properties because the β-Mg<sub>17</sub>Al<sub>12</sub> phase (present in Mg–Al alloys) softens at temperatures above 120 °C, leading to the deterioration of mechanical properties.<sup>2</sup> To overcome these limitations, Mg is usually alloyed with rare earth elements to form dispersed phases within the grains and along the grain boundaries which strengthens the base metal improving the performance.<sup>3–9</sup> The RE phases also favor the formation of protective films to improve the corrosion resistance of the alloy. The so-called “scavenger effect” of RE on the corrosion resistance of magnesium alloys trap the impurity elements such as Fe and Cu to form intermetallic compounds, thereby reducing their content in the alloy.<sup>10</sup>

The RE addition also affects the surface oxide film produced on magnesium alloys, which in turn enhance the corrosion resistance.<sup>9,10</sup> With this background, an attempt is made in this research work to synthesize and characterize a new Mg–Al alloy containing trace amounts of the RE element, gadolinium.

The microstructure and mechanical properties of binary Mg–Al alloys have been studied by Zheng et al.,<sup>11</sup> and it is seen that the properties increase with the Al content and the optimum results obtained are for 9 wt% Al. The microstructures of investigated Mg–Al alloys are composed of α-Mg solid solution, β-Mg<sub>17</sub>Al<sub>12</sub>, and the eutectic mixture (α-Mg + β-Mg<sub>17</sub>Al<sub>12</sub>). With the increase in Al content, the main structure of the alloys will change from the α-Mg solid solution to (α-Mg + β-Mg<sub>17</sub>Al<sub>12</sub>) the eutectic mixture.<sup>12</sup> By varying the cerium (Ce) mish metal addition (0, 1, 2, and 3 wt%), a study by Yizen et al.<sup>13</sup> on AZ91–xRE and Mg–6Al–xRE magnesium alloys shows that the hardness and high-temperature properties increase due to the presence of a rod-like Al<sub>11</sub>RE<sub>3</sub> precipitate phase and gradually reduced and refined Mg<sub>17</sub>Al<sub>12</sub>. Similar results are obtained by the addition of Ce mish metal (MM) and yttrium (Y) addition on Mg–9Al and Mg–4Al alloys resulting in the formation of rod-like Al<sub>4</sub>(Ce,La) for MM-added alloys and polygonal Al<sub>2</sub>Y for the Y-added alloys. The various phases formed like Al<sub>4</sub>(Ce,La) and Al<sub>2</sub>Y suppress the quantity of available Al to form Mg<sub>17</sub>Al<sub>12</sub>. Another study by Tomasz et al.<sup>14</sup> on the microstructure of the AE44 alloy shows the presence of the Al<sub>11</sub>RE<sub>3</sub> phase, Al<sub>2</sub>RE phase, and Al<sub>10</sub>RE<sub>2</sub>Mn<sub>7</sub>, which in turn attributes to better creep resistance of Mg–Al–RE alloys due to their high

Contributing Editor: Amit Bandyopadhyay

<sup>a)</sup>Address all correspondence to this author.

e-mail: utspillai@rediffmail.com

DOI: 10.1557/jmr.2017.348

melting temperatures. If the ratio of RE/Al (in wt%) is greater than 0.5, the Mg<sub>17</sub>Al<sub>12</sub> phase can be eliminated from the microstructure of Mg–Al alloys.<sup>14</sup>

Investigations by Chaubey on the effect of varying Ce on Mg<sub>90</sub>–Al<sub>10–x</sub>Ce<sub>x</sub> ( $x = 0, 1, 3, \text{ and } 5$  at.%) show that the addition of 1% Ce decreases the volume fraction of the Mg<sub>17</sub>Al<sub>12</sub> phase along with significant grain refinement. Further increase of Ce to 3 and 5% leads to a transformation of the Mg<sub>17</sub>Al<sub>12</sub> phase to Al<sub>11</sub>Ce<sub>3</sub> and Al<sub>2</sub>Ce phases. The ultimate compressive strength increases with increasing the Ce content and can be attributed to the smaller grain size of the alloy matrix due to the precipitation of high melting point intermetallic phases.<sup>15</sup> A study by Li et al.<sup>16</sup> on Mg– $x$ Al– $y$ Er alloys ( $x = 44.3, 44, 43.8, 43, 42$ ;  $y = 0, 0.5, 1, 3, 5$  wt%) shows that when the erbium (Er) content is less than 1.0 wt%, only Al<sub>3</sub>Er is present. When the Er content exceed 3.0 wt%, in addition to Al<sub>3</sub>Er phase, Mg<sub>17</sub>Al<sub>12</sub>–Mg eutectics are found in the matrix. The grain refinement effect is found to be critical in improving the microhardness, and the effect is prominent when the Er content is greater than 1 wt% (1–5 wt%). Corrosion and wear resistance are significantly enhanced by the addition of Er.

The microstructure of the Gd-added AZ71 magnesium alloy contains the  $\alpha$ -Mg matrix, eutectic  $\alpha$ (Mg) +  $\beta$ (Mg<sub>17</sub>Al<sub>12</sub>) phase, and Al<sub>2</sub>Gd phase. The microstructure of the alloy was seen to be refined and homogeneous by the Gd addition. The  $\beta$  phase volume fraction decreased and the  $\beta$ -phase was coarsened and congregated with the excessive Gd.<sup>17</sup> Hong et al.<sup>18</sup> investigated the effects of gadolinium (Gd) addition on the microstructure and mechanical properties of magnesium coatings; Mg–7.5Al– $x$ Gd ( $x = 0, 2.5, 5.0, \text{ and } 7.5$  wt%) was fabricated by laser cladding with wire feeding. The results indicated that Gd addition led to the formation of a cubic Al<sub>2</sub>Gd phase and suppressed the Mg<sub>17</sub>Al<sub>12</sub> phase. The laser clad coating containing 7.5 wt% Gd attained the highest microhardness and tensile properties at both room and high temperatures. The enhanced heat resistant capacity was attributed to the thermally stable Al<sub>2</sub>Gd particles.

This study is aimed to focus on the effect of varying Gd contents on the microstructure, hardness, tensile, corrosion, and wear resistance of the cast Mg–9Al alloy.

## II. EXPERIMENTAL

Pure Mg (99.95 wt%), pure Al (99.95 wt%), and Gd, procured from China, were used as raw materials to prepare the Mg–9Al– $x$ Gd alloys ( $x = 0, 0.5, 1, 2$  wt%). The raw materials were melted together in a mild steel crucible and were kept in an electric resistance furnace. Gas protection of the melt was ensured using SF<sub>6</sub> and Ar in the ratio 1:10. Finally, the melt was cast in a preheated (300 °C) cast iron mold and cooled in air to room

temperature. The compositions of the various alloys developed were analyzed through OES, Spectromax, Ametek (Meerbusch, Germany), and their codes are listed in Table I. The morphological observation and microstructural characterization of the specimens were performed using an optical microscope and Carl Zeiss Evo 18 scanning electron microscope (SEM; Carl Zeiss AG, Oberkochen, Germany). Cylindrical samples of 15 mm diameter and 10 mm height were machined from the castings and polished progressively with emery papers of different grades having 80, 100, 220, 400, and 600, and 1000 grits. After paper polishing, all the samples were cleaned using water and polished on a rotating disc of proprietary cloth (selvyte cloth) charged with a diamond paste of 6, 3, and 0.25  $\mu\text{m}$  particle size in a sequence. Filtered kerosene was used as the lubricating agent during cloth polishing. The polished samples cleaned with distilled water were found to be inefficient to remove surface contaminants. The phase determination of Mg–9Al– $x$ Gd alloys were analyzed by X-ray diffraction (XRD) and Energy Dispersive X-ray Spectroscopy (EDS) analysis. The XRD analysis was done on a Phillips PW 1710 Powder Diffractometer (Philips, Eindhoven, the Netherlands) with Cu-K $\alpha$  radiation (wave length = 1.54 Å). The X-ray source was operated at a voltage of 40 kV and at a current of 20 mA. The diffraction angle ( $2\theta = 10^\circ$  to  $90^\circ$ ) was selected such that all the major intense peaks of the phases expected in the sample were covered and a step size of  $0.0330^\circ$  were used. Subsequently, the XRD raw data were analyzed with the help of JCPDS data file and X'Pert software (PANalytical, Almelo, the Netherlands), which use the Bragg's law to identify the peaks of the constituent phases. The samples were subjected to solutionizing at 420 °C for 48 h followed by aging at 200 °C for 1 h, and the grain size was measured by linear intercept method, according to ASTM E112 standard.<sup>19</sup> The macrohardness tests for the Gd-containing alloys were performed using a Brinell hardness tester (Tinius Olsen, Horsham, Pennsylvania) with a 2.5 mm steel ball indenter under a loading force of 65 kgf for 20 s. Three values were taken for each sample and the mean values are reported. The tensile tests were conducted on an Instron Universal

TABLE I. The chemical composition of the studied Mg–9Al– $x$ Gd alloys.

Alloy code	Composition	Al (wt%)	Gd (wt%)	Fe (wt%)	Ni (wt%)	Cu (wt%)	Mg (wt%)
Alloy 1	Nominal	9	...	...	...	...	Rest
	Developed	8.55	...	0.0047	0.0001	0.0034	Rest
Alloy 2	Nominal	9	0.50	...	...	...	Rest
	Developed	8.54	0.57	0.0032	0.0001	0.0041	Rest
Alloy 3	Nominal	9	1.0	...	...	...	Rest
	Developed	9.10	1.25	0.0016	0.0001	0.0022	Rest
Alloy 4	Nominal	9	2.0	...	...	...	Rest
	Developed	8.77	1.97	0.0036	0.0001	0.0032	Rest

Testing Machine (Instron, Norwood, Massachusetts) using ASTM E8 specifications.<sup>20</sup> For each alloy, six tensile specimens with a gauge length of 50 mm were made and the tensile tests were carried out. The electrochemical properties were analyzed using a PGSTAT30 electrochemical workstation at room temperature ( $27 \pm 1$  °C) and a 3.5 wt% NaCl solution was used as the electrolyte. A three-electrode cell was used in this test, where the sample acted as the working electrode, a saturated calomel electrode (SCE) as the reference electrode, and a platinum sheet as the counter electrode. The scanning rate used was 2 mV/s. Based on the Tafel extrapolation method, the CH instrument software was used to measure the corrosion current density ( $i_{\text{corr}}$ ) of the specimens. The corrosion rate (CR) was calculated by measuring the average weight loss of three cylindrical samples each having 15 mm diameter and 15 mm height at the end of the immersion test by immersing the samples in 3.5 wt% NaCl solution for 3 days after which the corrosion products were removed by immersing the sample in chromic acid solution at room temperature for 30–40 min. The CR of the samples<sup>5</sup> was calculated using Eq. (1)

$$\text{CR} = \frac{8.76 \times 10^4 \times \Delta g}{A \times t \times \rho}, \quad (1)$$

Where,  $\Delta g$  is the weight loss in g,  $A$  is the surface area exposed in  $\text{cm}^2$ ,  $t$  is the total immersion time in hours, and  $\rho$  is the density of the alloy in  $\text{g/cm}^3$ .

The dry wear tests of the alloys were done on a pin-on-disc tester according to the ASTM G99 standard<sup>21</sup> at a sliding distance of 1800 m with loads varying from 1, 2, 3, 4, and 5 kg for 15 min against a disc of hardened EN31 high carbon alloy steel. The wear rate of three samples each was calculated using Eq. (2)

$$\text{Wear rate} = \text{volume loss (mm}^3\text{)}/\text{sliding distance (m)}. \quad (2)$$

### III. RESULTS AND DISCUSSION

#### A. Microstructure

The XRD pattern of the developed alloys (Fig. 1) mainly consists of peaks corresponding to the  $\alpha$ -Mg and  $\beta$ - $\text{Mg}_{17}\text{Al}_{12}$  phase of the bcc crystal structure. For the Gd-added alloys, the peaks corresponding to  $\text{Al}_2\text{Gd}$  (fcc crystal structure) are of low intensities due to relatively low quantities of Gd addition. Figure 2 shows the optical and SEM microstructures of the  $\text{Mg-9Al-xGd}$  alloys and the various phase formations. The phases are further confirmed using EDS analysis and are shown in Fig. 3. Some dispersed compounds and eutectic areas are seen in the alloys, which increase with increase in Gd content monotonically. The electronegativity difference

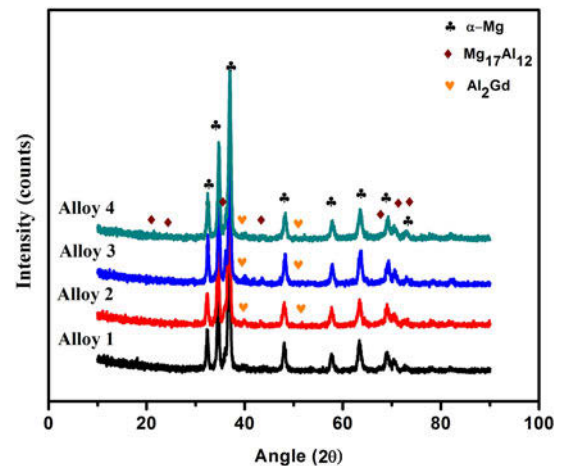


FIG. 1. XRD results of the studied alloys.

between two elements can be used to predict the possibility of formation of intermetallics. The larger the electronegativity difference, the stronger the bond and higher the possibility of intermetallics formation. As the electronegativity difference between Al and Gd is higher (0.3) than that between Mg and Gd (0.11), the formation of the Al–Gd phase is favored than that of the Mg–Gd phase in the Mg–Al–Gd system, and it is observed that the Gd addition decreased the quantity of the  $\text{Mg}_{17}\text{Al}_{12}$  phase.<sup>22–26</sup> The variation of  $\beta$  phase for the developed alloys is quantified using Image Analyzer. The volume fraction of  $\beta$  phase in Alloys 1, 2, 3, and 4 is found to be decreasing in the order 19.5, 17.2, 16.5, and 15.3%, respectively. The results indicate that the microstructure of the Mg–9Al alloy consist only of coarse  $\text{Mg}_{17}\text{Al}_{12}$  [Fig. 2(a)]. With the addition of 0.5 wt% Gd, the microstructure of the Mg–9Al–0.5Gd alloy shows granular  $\text{Al}_2\text{Gd}$  intermetallic particles sparsely distributed in the Mg–Al matrix [Fig. 2(b)]. Increasing the content of Gd to 1 and 2 wt% in the Mg–9Al–xGd alloy increases the  $\text{Al}_2\text{Gd}$  phase distribution in the matrix. As seen from the optical microstructures, it can be seen that the microstructure becomes refined with decrease in the volume fraction of  $\text{Mg}_{17}\text{Al}_{12}$ .

#### B. Mechanical properties

The mechanical properties comprising of macrohardness, ultimate tensile strength (UTS), yield strength (YS), and elongation (Elon) of as-cast Mg–9Al–xGd alloys at RT and at 150 °C are presented in Table II. Addition of Gd shows significant beneficial effects on mechanical properties and the lattice constant of Gd is very similar to that of Mg. The lattice constants of Gd and Mg are  $a = 0.36360$  and  $c = 0.57826$  nm and  $a = 0.32094$  and  $c = 0.52104$  nm, respectively. Due to size difference between Gd (0.233 nm) and Mg (0.162 nm) atoms, Gd is difficult to solid-solute in the Mg alloy but tends to form

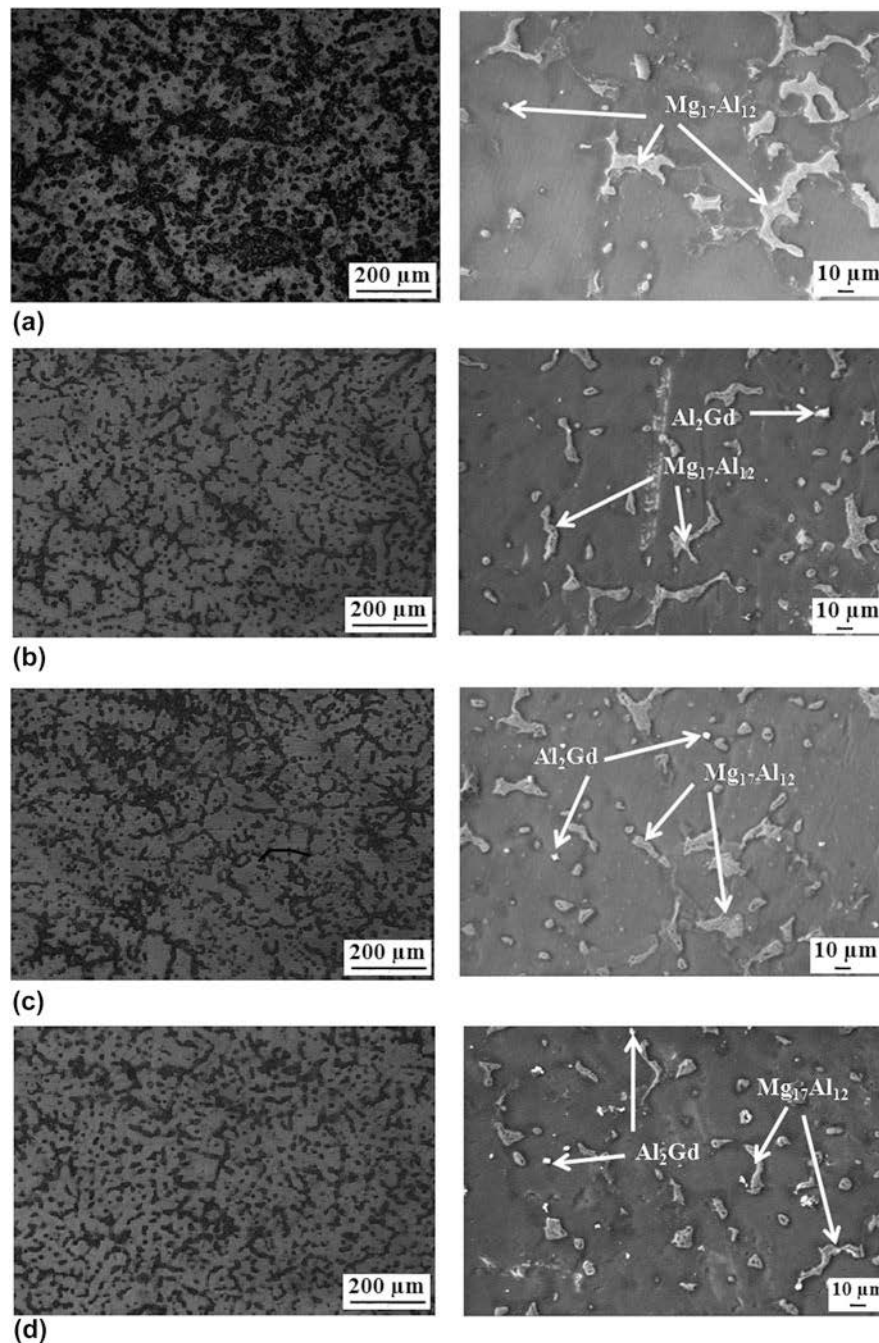
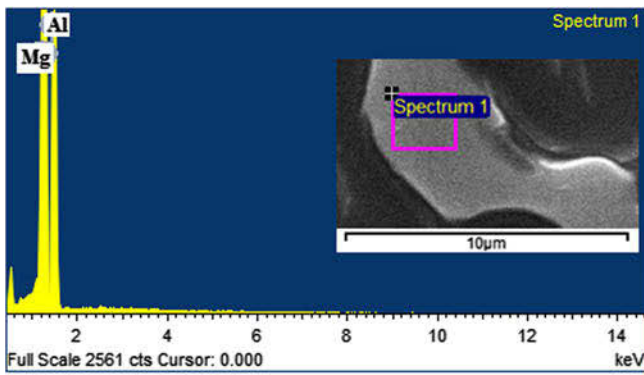


FIG. 2. Optical and SEM microstructures of (a) Alloy 1, (b) Alloy 2, (c) Alloy 3, and (d) Alloy 4.

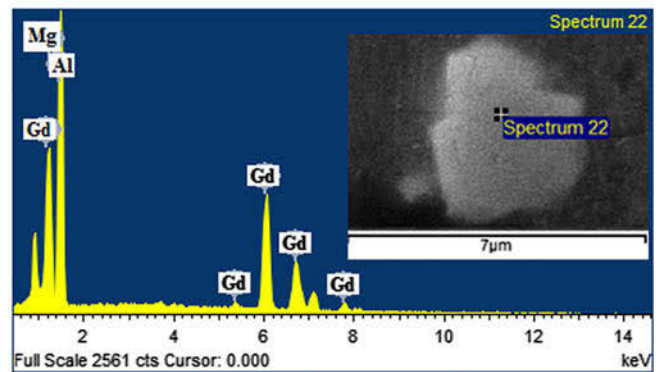
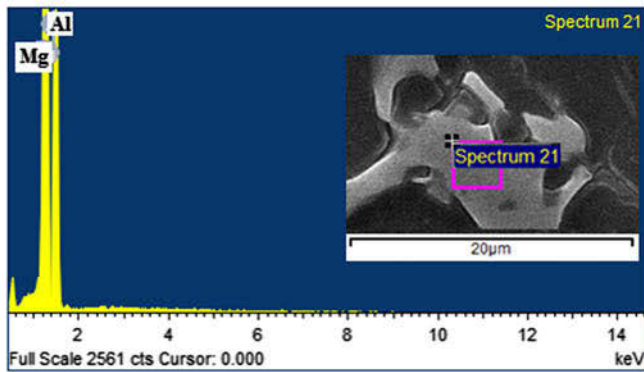
rare earth compounds. It is seen that by Gd addition, the hardness value of the alloy increases from 50.1 BHN, and the highest value of 66.2 BHN is obtained for Alloy 4. Moreover, the hardness of alloys is increased by increasing the percentage of Gd addition, mainly due to the increase in volume of the  $\text{Al}_2\text{Gd}$  phase and the Gd dissolution into the matrix. Moderate improvement in UTS (8%) and YS (12%) is noticed with 0.5 wt% Gd-added alloy, and this can be attributed to solid solution strengthening and reduction in the stress

concentration by refining the microstructure.<sup>14,15,24,27</sup> Alloy 4 at room temperature shows 27 and 36% increase of UTS and YS, respectively, compared to Alloy 1 due to the formation of the  $\text{Al}_2\text{Gd}$  phase which restricts the dislocation movement and grain boundary sliding.<sup>26–34</sup> The strength of the grain boundary is greater than the strength of the grain at room temperature. During tensile deformation, the dislocations move inside the grain until they reach the grain boundary, where the motion is opposed. More dislocations get piled up as a cluster at

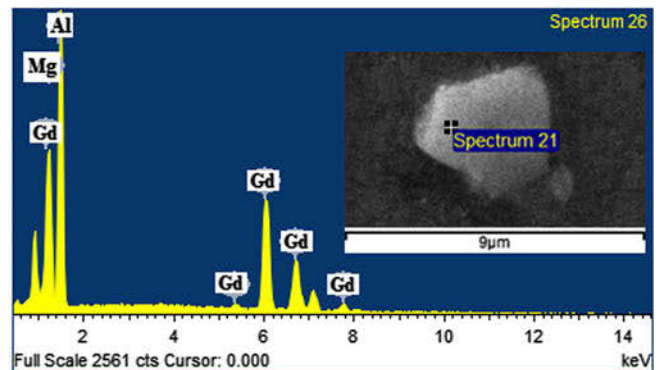
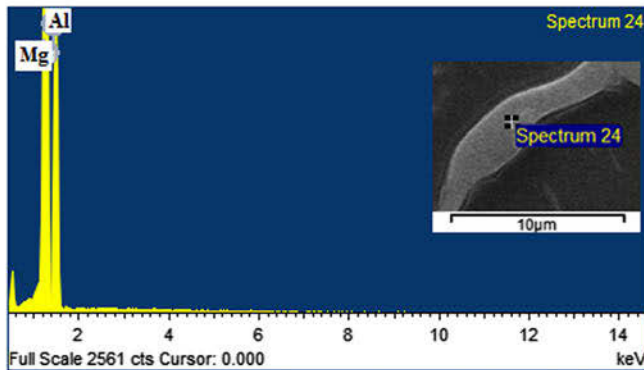


Alloy code	Mg (at%)	Al(at%)	Gd (at%)	Calculated phase
Alloy 1	69.40	30.60		$Mg_{17}Al_{12}$
Alloy 2	65.14	34.86		$Mg_{17}Al_{12}$
	24.73	54.95	20.32	$Al_2Gd$
Alloy 3	68.23	31.77		$Mg_{17}Al_{12}$
	24.90	55.65	19.45	$Al_2Gd$
Alloy 4	69.73	30.27		$Mg_{17}Al_{12}$
	22.68	55.88	21.44	$Al_2Gd$

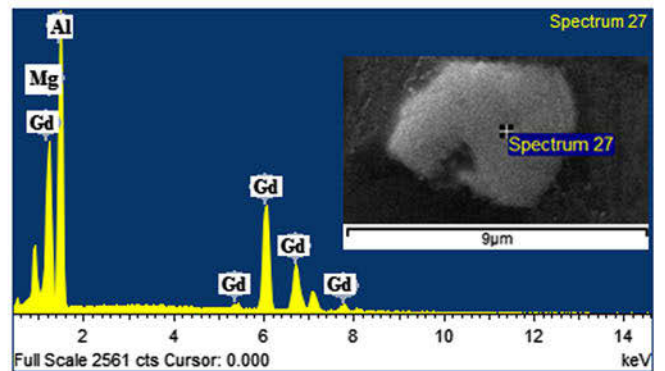
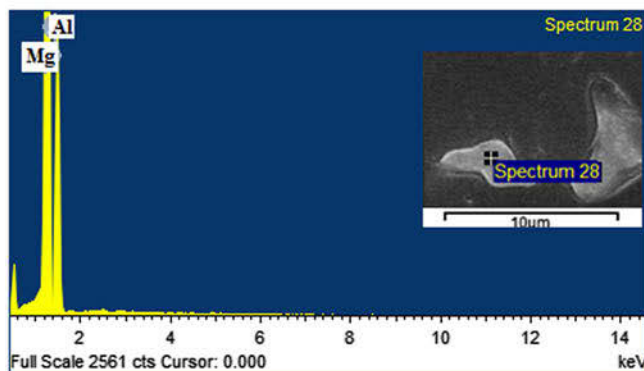
(a)



(b)



(c)



(d)

FIG. 3. EDS results of (a) Alloy 1, (b) Alloy 2, (c) Alloy 3, and (d) Alloy 4.

TABLE II. Mechanical properties of the studied Mg–9Al–xGd alloys.

Alloy code	Hardness (BHN)	RT			HT (150 °C)		
		UTS (MPa)	YS (MPa)	Elon (%)	UTS (MPa)	YS (MPa)	Elon (%)
Alloy 1	50.1 (±1.5)	165.21 (±13.52)	84.61 (±14.57)	4.0 (±0.1)	115.87 (±5.68)	58.10 (±7.75)	5.5 (±0.4)
Alloy 2	53.9 (±2.8)	179.33 (±12.34)	96.22 (±12.23)	4.2 (±0.2)	143.44 (±10.67)	65.22 (±9.43)	5.6 (±0.3)
Alloy 3	60.3 (±1.2)	187.75 (±13.31)	112.42 (±9.65)	4.3 (±0.5)	152.02 (±3.43)	69.32 (±5.21)	5.9 (±0.4)
Alloy 4	66.2 (±1.6)	210.03 (±10.73)	116.21 (7.17)	4.6 (±0.7)	159.34 (±9.49)	74.22 (±5.53)	6.4 (±0.5)

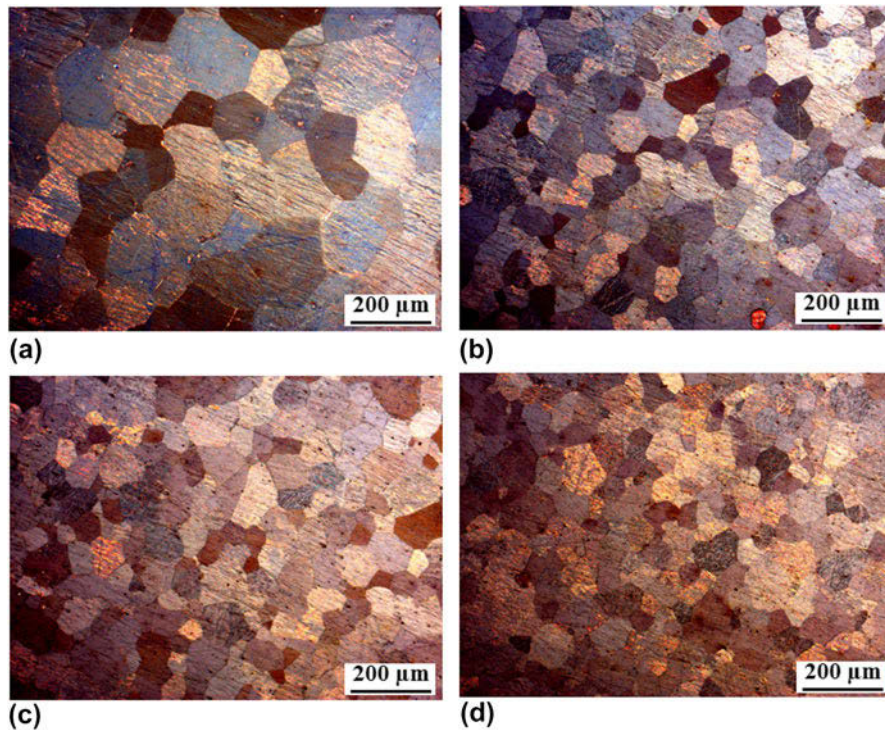


FIG. 4. Grain size of (a) Alloy 1, (b) Alloy 2, (c) Alloy 3, and (d) Alloy 4.

the boundaries thereby generating a repulsive stress field. Then the dislocations will apply the driving repulsive force to reduce the energy for the dislocation diffusing across the boundary. The higher the repulsive stress applied to move the dislocation, the higher the YS would be.<sup>16</sup> So, a decrease in the grain size favors the increment of yield strength. The average grain size is seen to be around 200, 140, 120, and 100  $\mu\text{m}$  for the Alloys 1, 2, 3, and 4, respectively, (Fig. 4). At 150 °C, the maximum strength values (UTS & YS) are obtained for Alloy 4 (159.34 and 74.22 MPa, respectively). In Alloy 1,  $\text{Mg}_{17}\text{Al}_{12}$  is the main strengthening phase, which has a low melting point of 462 °C and poor thermal stability. The  $\text{Mg}_{17}\text{Al}_{12}$  phase can readily coarsen and soften at the temperatures above 120 °C. The cubic crystal structure of  $\text{Mg}_{17}\text{Al}_{12}$  is incoherent with the h.c.p. magnesium matrix, leading to the fragility of the Mg:  $\text{Mg}_{17}\text{Al}_{12}$  interface. All of the above lead to the poor high temperature tensile properties of Mg–9Al alloys at 150 °C.<sup>12,13</sup> It is seen that the addition of Gd helps in

improving the strength at 150 °C. The maximum strength values obtained for Alloy 4 is possibly due to the formation of thermally stable intermetallic  $\text{Al}_2\text{Gd}$  precipitates. At higher temperatures, the strength of the grain boundaries are weak compared to the strength of the grains, and fine-grain strengthening would be less effective, but they do serve as an obstacle during dislocation motion. The presence of thermally stable  $\text{Al}_2\text{Gd}$  particles restrict the dislocation motion and increase the alloy density at both room and high temperatures. The more the  $\text{Al}_2\text{Gd}$  disperses, the higher tensile and YS would it attain.<sup>18</sup>

### C. Corrosion studies

#### 1. Electrochemical test

The potentiodynamic polarization behavior of the developed alloys are depicted in Fig. 5(a) and the polarization features such as  $i_{\text{corr}}$  and  $E_{\text{corr}}$  of the alloys, measured from polarization curves, are presented in Table III. The  $E_{\text{corr}}$  values of the investigated binary

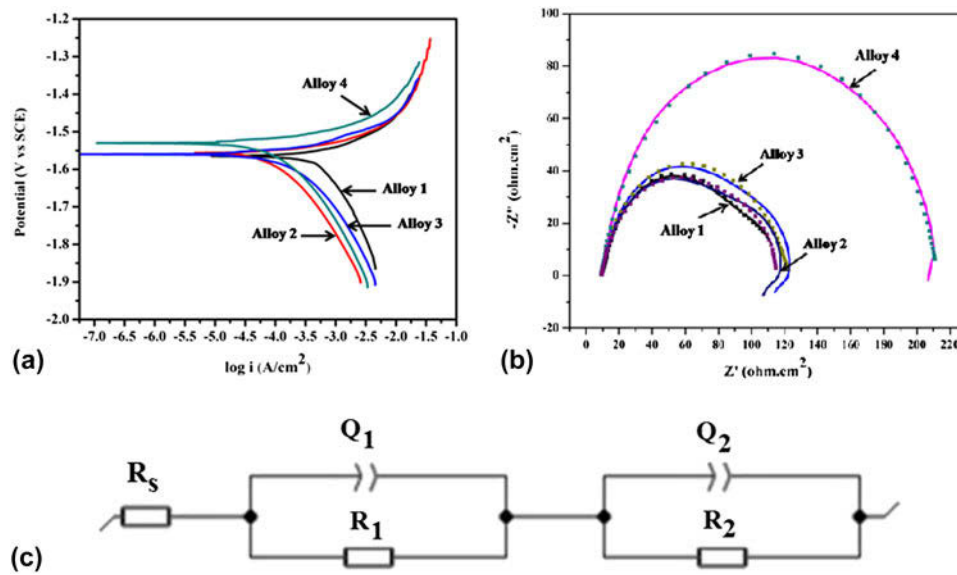
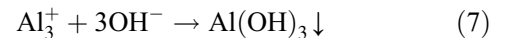
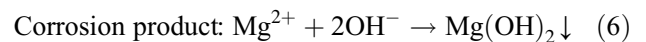
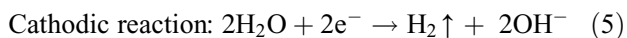
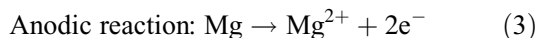


FIG. 5. (a) Tafel plot, (b) Nyquist plot, and (c) equivalent circuit model of the studied alloys.

TABLE III. Electrochemical results of the studied Mg–9Al–xGd alloys.

	Alloy 1	Alloy 2	Alloy 3	Alloy 4
$i_{\text{corr}}$ (mA/cm <sup>2</sup> )	1.5350 ( $\pm 0.0311$ )	0.2756 ( $\pm 0.0213$ )	0.1024 ( $\pm 0.0423$ )	0.0854 ( $\pm 0.0046$ )
$E_{\text{corr}}$ (V)	–1.565 ( $\pm 0.024$ )	–1.556 ( $\pm 0.033$ )	–1.560 ( $\pm 0.010$ )	–1.530 ( $\pm 0.036$ )

alloys varied between –1.565 and –1.530 V. It is seen that the Gd additions have shifted the cathodic portion of the curves toward lower current densities. The corrosion current is an actual measure of the corrosion rate, representing the material's corrosion behavior in a greater degree. The current density values are seen to decrease with increase in the amount of Gd addition, suggesting that there is an increase in corrosion resistance. It is seen in Table III that the corrosion current densities ( $i_{\text{corr}}$ ) of the alloys with Gd addition is lower than those of Alloy 1 upto 2 wt% with appreciable reduction for Alloy 4, which is two orders of magnitude lower than that of Alloy 1, implying that Alloy 4 has the highest corrosion resistance. The corrosion process of Mg–Al alloys in the NaCl solution undergoes two main reactions. One is the anodic dissolution reaction and the other is the cathodic hydrogen evolution reaction.<sup>34</sup> The reaction equations are listed in Eqs. (3)–(7).



The electrochemical results indicate that Gd is effective in enhancing the corrosion resistance of Mg–Al intermetallic alloys by suppressing the hydrogen evolution.<sup>16,27</sup> Grain boundaries play an important role in affecting an alloy's corrosion resistance. Some investigations show that the grain boundaries act as the hindrance for corrosion due to the second phase and always have better corrosion resistance.<sup>34–37</sup> When the Gd content reaches to 2.0 wt%, the grain size is smaller compared to the other alloys imparting the best corrosion resistance. The variations in corrosion current of the Gd added alloys is due to the reduction of Mg<sub>17</sub>Al<sub>12</sub> or compositional homogenization. The Mg<sub>17</sub>Al<sub>12</sub> precipitates act as microcathodes, causing internal galvanic corrosion thereby accelerating the corrosion process.<sup>33</sup> When gadolinium is added, the Al present in the alloys is utilized to form Al–Gd phases thereby lowering the Al content available to form Mg<sub>17</sub>Al<sub>12</sub> precipitates. It has been validated that the potential difference between Mg<sub>17</sub>Al<sub>12</sub> and the  $\alpha$  phase is relatively larger than the potential difference between the Al<sub>2</sub>Y and  $\alpha$  phase.<sup>38</sup> Similarly, the microgalvanic cathode caused by the

potential difference will be weakened with  $\text{Al}_2\text{Gd}$  gradually replacing  $\text{Mg}_{17}\text{Al}_{12}$ . Eventhough the  $\text{Al}_2\text{Gd}$  acts as the main corrosion resisting phase, it also acts as the cathode, inducing galvanic effects, because the  $\text{Al}_2\text{Gd}$  surrounding the Mg matrix gets preferentially dissolved, suggesting the cathodic nature of the same relative to the Mg matrix.<sup>3,34–39</sup> But the additions upto 2% do not produce many such microelectrodes and results in corrosion resistance.

The electrochemical impedance spectroscopy (EIS) behavior of the studied samples is represented as the Nyquist plot; the simulated fittings are shown in Fig. 5(b) and are found to be well fitted with the experimental spectra. The diameter of the capacitive semicircle in the nyquist plot is highly associated with the corrosion resistance; larger diameter implies a higher corrosion resistance.<sup>40</sup> Among the studied alloys, Alloy 4 exhibited a larger diameter whereas Alloy 1 showed the lowest diameter, indicating that corrosion resistance of alloys increased with increase in the Gd content. The fitted EIS values of the experimental allos are summarized in Table IV. In the equivalent circuit [Fig. 5(c)],  $R_s$  represents the solution resistance between the reference electrode and specimen. A constant phase element, usually represented as  $Q$ , is an equivalent electrical circuit component that models the behavior of a double layer that is an imperfect capacitor.  $Q_1$  and  $Q_2$  represent the two constant phase elements which are used to obtain a good fit, considering the inhomogeneous reaction rates at the electrode surface, electrode surface roughness, varying thickness, and nonuniform current distribution during corrosion.<sup>41</sup>  $R_1$  and  $R_2$  are the respective resistance elements corresponding to  $Q_1$  and  $Q_2$ . The  $R$  values of the samples [in the high frequency domain ( $R_1$ )] increased in the following order: Alloy 1 < Alloy 2 < Alloy 3 < Alloy 4. Among the studied alloys, Alloy 4 showed the highest resistance indicating its increased corrosion resistance. The  $Q$  value is related to the corrosion reaction area, i.e., low  $Q$  value implies that a relatively low area of the exposed surface is corroded. The fitted values of  $Q$  show a continuous decrease in the following order: Alloy 1 > Alloy 2 > Alloy 3 > Alloy 4. The thin layer of oxide due to the interaction of the alloy

surface with air and the corrosion product formed during the corrosion act as a protective cover to the surface in the NaCl solution to some extent. The similar values of  $Q$  observed with all the tested alloys indicated that the protection offered by the corrosion product was similar. In general, for bare substrates, the high frequency capacitive loop represents the formation of oxides or hydroxides at the metal–solution interface as the result of corrosion occurring during the test. The values of ‘ $n$ ’ for all the alloys are close to unity, indicating a capacitance behavior. However the deviation observed in the ‘ $n$ ’ values is normally due to nonuniform current distribution. The presence of the inductive loop indicates the occurrence of pitting corrosion in the samples.

## 2. Immersion test

To substantiate the electrochemical results, immersion tests have been done by immersing all the alloys in 3.5 wt% NaCl solution for 72 h. Figure 6 shows the macro images of corroded samples of Alloys 1, 2, 3, and 4 for a varying time of 6, 24, 48, and 72 h. With increasing the immersion time, the Gd-added alloys are seen to be less corroded. The surface becomes covered with loose white corrosion products, which are assumed to be  $\text{Mg}(\text{OH})_2$ . The corrosion initiation in the various developed alloys can be clearly seen after 6 h of immersion. Corrosion initiates from the edges in all samples due to irregularity and the sharp edge. After 24 h, Alloy 1 shows pitting and uniform corrosion, and almost 70% of the area is corroded. For Alloys 2 and 3, localized pitting corrosion is seen at almost 40 and 20% of the exposed area, respectively. For Alloy 4, the initiation of corrosion can be seen, which is still less when compared to the base alloy. After 48 h, a similar trend as 24 h is seen for all alloys. It is seen that the corrosion behavior of Alloys 2 and 3 are almost similar in nature. After 72 h, the metallic luster of Alloy 1 is completely lost while Alloys 2 and 3 show similar uniform pitting corrosion throughout the surface. As seen from Fig. 6, under the same test conditions, the metallic luster is quite retained in Alloy 4 and suffered less corrosion compared to the other alloys, which may be due to a more uniform and compact corrosion product film formation. The main corrosion form of magnesium alloy is usually pitting corrosion, and from the thermodynamics theory, due to different corrosion potentials, the polarization effect of  $\beta$  phase influences the  $\alpha$  phase thereby increasing the CR of the  $\alpha$  phase and hence corrosion pits are easily formed in the  $\alpha$  phase.<sup>35,36</sup> With the addition of Gd, the corrosion potential moves to the negative direction and due to the atomic size difference between Gd and Mg atoms, Gd becomes difficult to solid-solute in the magnesium alloy and forms rare earth compounds. Another effect of Gd addition is grain

TABLE IV. The fitted EIS values of the experimental alloys.

	Alloy 1	Alloy 2	Alloy 3	Alloy 4
$R_s$ ( $\Omega \text{ cm}^2$ )	9.467	9.356	9.714	9.549
$Q_1$ ( $\text{s}^n/\Omega \text{ cm}^2$ )	$22.17 \times 10^{-6}$	$26.27 \times 10^{-6}$	$35.06 \times 10^{-6}$	$54.16 \times 10^{-6}$
$n_1$	0.9656	0.7833	0.8696	0.9662
$R_1$ ( $\Omega \text{ cm}^2$ )	65.49	79.42	82.66	100.2
$Q_2$ ( $\text{s}^n/\Omega \text{ cm}^2$ )	$23.06 \times 10^{-6}$	$34.26 \times 10^{-6}$	$37.21 \times 10^{-6}$	$45.64 \times 10^{-6}$
$n_2$	0.8909	0.8956	0.9745	0.8868
$R_2$ ( $\Omega \text{ cm}^2$ )	33.41	39.83	42.83	70.72



refinement which reduces the micro-galvanic effect. Gd also acts as a purifying element, by removing the impurities in the alloy and hence the corrosion resistance of magnesium alloys are enhanced.<sup>3,35-38</sup> The gap in between the  $\beta$  phases is large in Alloy 1 compared to the other alloys and is not effectively blocked by the corrosive products formed between the  $\beta$  and  $\alpha$  phase,

resulting in pits and increased corrosion rate. The small grain size and narrow gap between precipitates in Alloy 4 improve the passive film, thereby inhibiting anodic dissolution and preventing the occurrence of pits.

Figure 7(a) shows the variation of the CR (in mm/year) of experimental alloys as a function of immersion time in 3.5 wt% NaCl solution. It is seen that the CR of all alloys

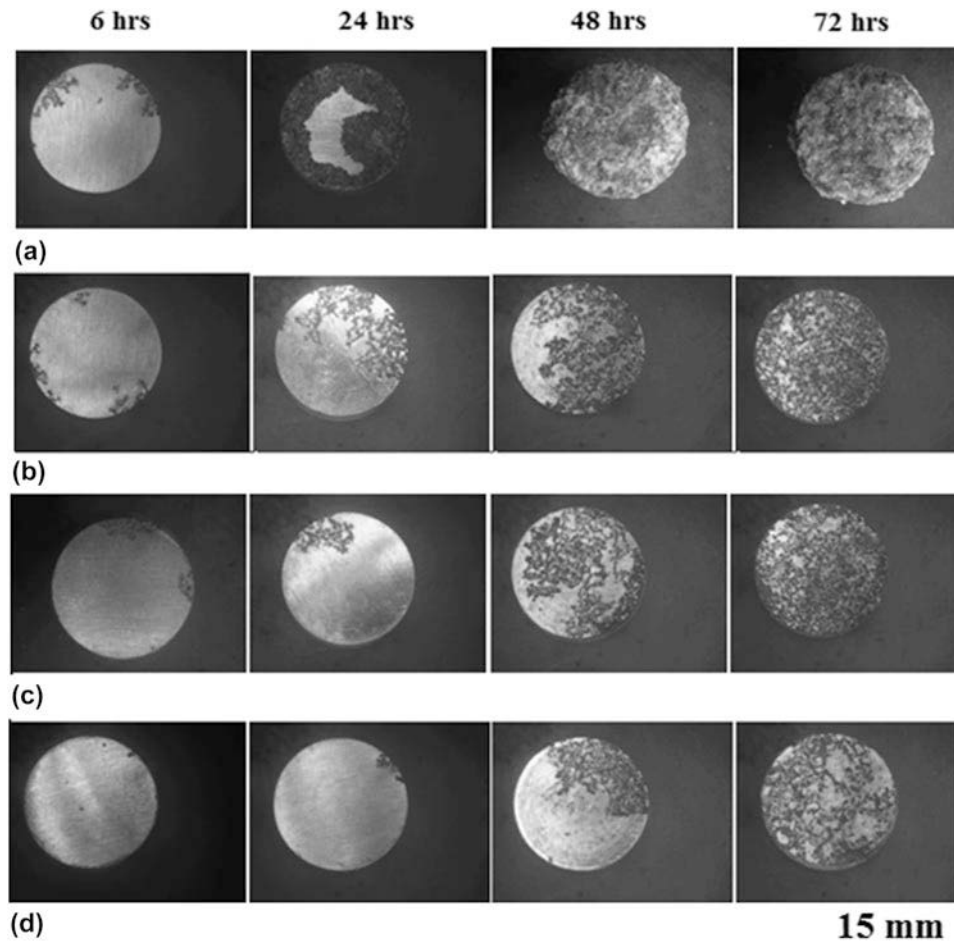


FIG. 6. Macro images of the corroded alloys (a) Alloy 1, (b) Alloy 2, (c) Alloy 3, and (d) Alloy 4 kept at different immersion times.

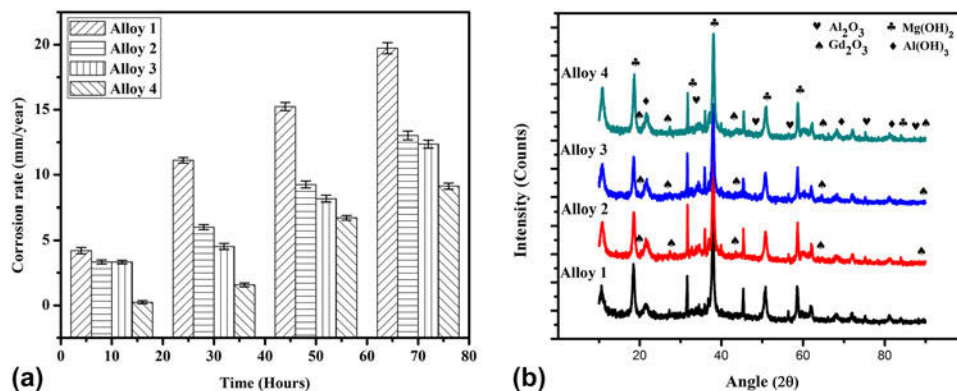


FIG. 7. (a) Corrosion rate of the alloys for different time and (b) XRD results of the corroded alloys.

increase with respect to the immersion time. In the case of Gd-added alloys, it is seen that the CR is minimal, especially in the case of Alloy 4 when compared to the base alloy which indicates the positive effect of Gd addition. From the XRD results [Fig. 7(b)], it is seen that various hydroxide and oxide layers like  $\text{Mg}(\text{OH})_2$ ,  $\text{Al}(\text{OH})_3$ ,  $\text{Al}_2\text{O}_3$ , and  $\text{Gd}_2\text{O}_3$  seem to have developed after the immersion test. It is suggested that adding RE to Mg alloys may improve the passivation of the alloy via incorporation of REs in the surface film of  $\text{Mg}(\text{OH})_2$  or stabilize corrosion product films to suppress further corrosion.<sup>42,43</sup> The improved corrosion resistance of the

Alloy 4 can be explained as the incorporation of oxidized Gd by substituting magnesium cations thereby preventing the incorporation of chloride anions in the  $\text{Mg}(\text{OH})_2$  lattice, resulting in the decreased susceptibility of the passive film breakdown. The corrosion resistance with Gd addition is mainly due to (i) improved film stability surrounding the  $\beta\text{-Mg}_{17}\text{Al}_{12}$  phase due to the formation of the  $\text{Al}_2\text{Gd}$  phase at the grain boundaries, (ii) low volume fraction of the  $\beta\text{-Mg}_{17}\text{Al}_{12}$  phase, (iii) presence of more protective oxide films, and (iv) reduction in grain size.

#### D. Dry wear resistance

As seen from the hardness data, the Gd addition make the alloy harder, which is mainly due to the formation of the  $\text{Al}_2\text{Gd}$  phase, whose volume fraction increased with increasing the Gd concentration. Due to the Gd addition, the  $\text{Mg}_{17}\text{Al}_{12}$  phase is substituted by a more thermodynamically favorable  $\text{Al}_2\text{Gd}$  phase. The increase in hardness would directly increase the wear resistance of the alloys.<sup>16,44-47</sup> The weight loss of samples with varying Gd additions are measured using the pin-on-disc tester, and the calculated wear rate is shown in Fig. 8. It is observed that there is a considerable decrease in the weight loss by increasing the content of Gd, which is consistent with the increase in hardness due to the formation of a harder  $\text{Al}_2\text{Gd}$  phase, whose volume fraction increases with the increase in Gd. It is seen that the weight loss of Alloy 1 is about 18% more than that of Alloy 4. The enhanced wear resistance can also be attributed to the higher thermal stability of the  $\text{Al}_2\text{Gd}$

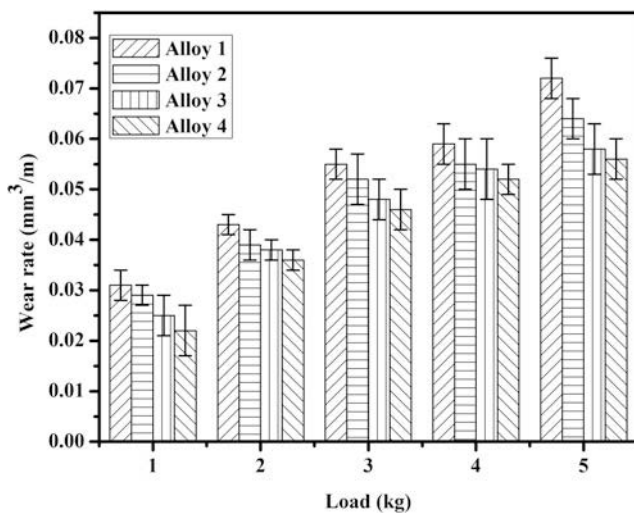


FIG. 8. Wear rate of the studied alloys at corresponding loads.

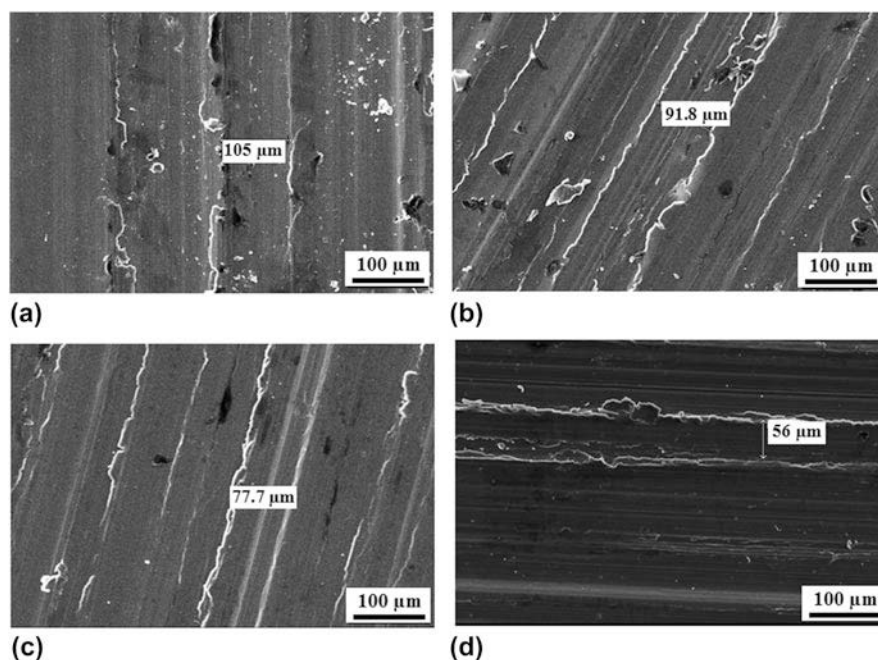


FIG. 9. SEM micrographs of the worn (a) Alloy 1, (b) Alloy 2, (c) Alloy 3, and (d) Alloy 4 tested at 5 kg.

phase, compared to that of  $Mg_{17}Al_{12}$ . During the dry wear test, due to increase in the sample surface temperature, softening occurs for materials with low-melting temperatures. The thermally stable  $Al_2Gd$  phase effectively resists wear under such testing conditions. The wear morphology results of the test specimens at 5 kg load are shown in Fig. 9. The wear scar width (WSW) of the as-cast Mg–9Al alloy is 105  $\mu m$ . Large pieces of the alloy are seen to peel off from the matrix, and the cracks propagate in a straightline. Taking into consideration the hardness and the second phase, the Alloy 4 has the lowest WSW value of 56  $\mu m$ , indicating its higher wear resistance.

#### IV. CONCLUSIONS

From this study, it is understood that the addition of the rare earth element Gd has an effect on the microstructure, mechanical, corrosion, and wear behavior of the Mg–Al alloy. The main conclusions are (i) when Gd is added in varying wt%, a thermally stable  $Al_2Gd$  phase is formed along with the  $\beta$ - $Mg_{17}Al_{12}$  in the matrix, (ii) the hardness of the Gd-containing alloys is evidently improved by the Gd addition, and the maximum hardness of 66.2 BHN is obtained with 2.0 wt% Gd addition, (iii) the tensile properties of the alloys are enhanced by the Gd addition due to the presence of thermally stable intermetallic  $Al_2Gd$  precipitates at the grain boundaries, which effectively suppress the dislocation motion and grain boundary sliding, and (iv) corrosion and wear resistance are significantly enhanced by the addition of Gd. The Mg–9Al–2Gd alloy has the lowest  $i_{corr}$  and the most negative  $E_{corr}$ , which points that this alloy has the strongest suppression effect in cathodic hydrogen evolution and the highest corrosion resistance. The WSW of the Mg–9Al–2Gd alloy is decreased by 46%, compared with the cast Mg–9Al alloy, indicating its enhanced wear resistance.

#### ACKNOWLEDGMENTS

The authors would like to thank the Council of Scientific and Industrial Research (CSIR), India AcSIR and CSIR – Network Project (SURE) for the financial support and the Director, National Institute for Interdisciplinary Science and Technology (NIIST), Trivandrum for providing an opportunity to conduct the study. Heartfelt thanks for all those who had been a source of constant motivation and encouragement during the course of this work.

#### REFERENCES

1. I.J. Polmear: Magnesium alloys. In *Light Alloys*, 4th ed., I.J. Polmear, ed. (Butterworth-Heinemann, Oxford, 2005); p. 237.
2. R. Muraliraja, H. Vetrivel, and R. Elansezhian: Synthesis and characterization of magnesium alloy added with yttrium and to

study the microstructure and mechanical properties. *Int. J. Eng. Innov. Technol.* **7**, 388 (2013).

3. W. Liu, F. Cao, L. Chang, Z. Zhang, and J. Zhang: Effect of rare earth element Ce and La on corrosion behavior of AM60 magnesium alloy. *Corros. Sci.* **51**, 1334 (2009).
4. J.L. Wang, H.W. Dong, L.D. Wang, Y.M. Wu, and L.M. Wang: Effect of hot rolling on the microstructure and mechanical properties of Mg–5Al–0.3Mn–2Nd alloy. *J. Alloys Compd.* **507**, 178 (2010).
5. A. Boby, A. Srinivasan, U.T.S. Pillai, and B.C. Pai: Mechanical characterization and corrosion behavior of newly designed Sn and Y added AZ91 alloy. *Mater. Des.* **88**, 871 (2015).
6. A. Boby, A. Srinivasan, U.T.S. Pillai, and B.C. Pai: Effect of antimony and yttrium addition on the high temperature properties of AZ91 magnesium alloy. *Procedia Eng.* **55**, 98 (2013).
7. H. Yokobayashi, K. Kishida, H. Inui, M. Yamasaki, and Y. Kawamura: Enrichment of Gd and Al atoms in the quadruple close packed planes and their in-plane long-range ordering in the long period stacking-ordered phase in the Mg–Al–Gd system. *Acta Mater.* **59**, 7287 (2011).
8. L.K. Singh, A. Srinivasan, U.T.S. Pillai, M.A. Joseph, and B.C. Pai: The effect of yttrium addition on the microstructure and mechanical properties of Mg alloys. *Trans. Indian Inst. Met.* **68**, 331 (2015).
9. S. Luo, G. Yang, S. Liu, J. Wang, J. Li, and W. Jie: Microstructure evolution and mechanical properties of directionally solidified Mg–xGd ( $x = 0.8, 1.5, \text{ and } 2.5$ ) alloys. *Mater. Sci. Eng., A* **662**, 241 (2016).
10. W. Liu, F. Cao, L. Zhong, L. Zheng, B. Jia, Z. Zhang, and J. Zhang: Influence of rare earth element Ce and La addition on corrosion behavior of AZ91 magnesium alloy. *Mater. Corros.* **60**, 795 (2009).
11. Z. Wei-Chao, L. Shuang-Shou, T. Bin, and Z. Da-Ben: Microstructure and properties of Mg–Al binary alloys. *China Foundry* **3**, 270 (2006).
12. L. Zhang, Z.Y. Cao, Y.B. Liu, G.H. Su, and L.R. Cheng: Effect of Al content on the microstructures and mechanical properties of Mg–Al alloys. *Mater. Sci. Eng., A* **508**, 129 (2009).
13. Y. Lu, Q. Wang, X. Zeng, W. Ding, C. Zhai, and Y. Zhu: Effects of rare earths on the microstructure, properties and fracture behavior of Mg–Al alloys. *Mater. Sci. Eng., A* **278**, 66 (2000).
14. T. Rzychon, A. Kielbus, and L. Litynska-Dobrzynska: Microstructure, microstructural stability and mechanical properties of sand-cast Mg–4Al–4RE alloy. *Mater. Charact.* **83**, 21 (2013).
15. A.K. Chaubey, S. Scudino, K.G. Prashanth, and J. Eckert: Microstructure and mechanical properties of Mg–Al based alloy modified with cerium. *Mater. Sci. Eng., A* **625**, 46 (2015).
16. Y. Li, Y. Wei, L. Hou, C. Guo, and P. Han: Effect of erbium on microstructures and properties of Mg–Al intermetallic. *J. Rare Earths* **32**, 1064 (2014).
17. K.J. Li: Effects of Gd on microstructure of Mg–Al magnesium alloy. *Adv. Mater. Res.* **821–822**, 860 (2013).
18. H. Chena, K. Zhanga, C. Yaoa, J. Dong, Z. Li, and C. Emmelmann: Effect of  $Al_2Gd$  on microstructure and properties of laser clad Mg–Al–Gd coatings. *Appl. Surf. Sci.* **330**, 393 (2015).
19. ASTM E112-13 Standard Test Methods for Determining Average Grain Size, ASTM International, West Conshohocken, PA, 2013. <https://doi.org/10.1520/E0112>.
20. ASTM E8/E8M-16a Standard Test Methods for Tension Testing of Metallic Materials, ASTM International, West Conshohocken, PA, 2016. [https://doi.org/10.1520/E0008\\_E0008M-16A](https://doi.org/10.1520/E0008_E0008M-16A).
21. ASTM G99-17 Standard Test Method for Wear Testing with a Pin-on-Disk Apparatus, ASTM International, West Conshohocken, PA, 2017. <https://doi.org/10.1520/G0099-17>.
22. L.Y. Wei and G.L. Dunlop: The solidification behaviour of Mg–Al–rare earth alloys. *J. Alloys Compd.* **232**, 264 (1996).

23. T. Rzychon and A. Kielbus: Effect of rare earth elements on the microstructure of Mg–Al alloys. *JAMME* **17**, 149 (2006).
24. H.L. Chen, L. Lin, P.L. Mao, and Z. Liu: Phase stability, electronic, elastic and thermodynamic properties of Al–RE intermetallics in Mg–Al–RE alloy: A first principles study. *J. Magnesium Alloys* **3**, 197 (2015).
25. S.M. Zhu, M.A. Gibson, J.F. Nie, M.A. Eastona, and T.B. Abbott: Microstructural analysis of the creep resistance of die-cast Mg–4Al–2RE alloy. *Scr. Mater.* **58**, 477 (2008).
26. S.M. Jo, K.C. Park, B.H. Kim, H. Kimura, S.K. Park, and Y.H. Park: Investigation on the microstructure and mechanical properties of Mg–Al–Yb alloys. *Mater. Trans.* **52**, 1088 (2011).
27. F. Lu, A. Ma, J. Jiang, Y. Guo, D. Yang, D. Song, and J. Chen: Significantly improved corrosion resistance of heat-treated Mg–Al–Gd alloy containing profuse needle-like precipitates within grains. *Corros. Sci.* **94**, 171 (2015).
28. X. Wang, W. Du, K. Liu, Z. Wang, and S. Li: Microstructure, tensile properties and creep behaviors of as-cast Mg–2Al–1Zn– $x$ Gd ( $x = 1, 2, 3$ , and 4 wt%) alloys. *J. Alloys Compd.* **522**, 78 (2012).
29. Q. Peng, H. Dong, Y. Wu, and L. Wang: Age hardening and mechanical properties of Mg–Gd–Er alloy. *J. Alloys Compd.* **456**, 395 (2008).
30. J. Wang, L. Wang, J. An, and Y. Liu: Microstructure and elevated temperature properties of die-cast AZ91– $x$ Nd magnesium alloys. *J. Mater. Eng. Perform.* **17**, 725 (2008).
31. F. Mert, A. Ozdemir, K.U. Kainer, and N. Hort: Influence of Ce addition on microstructure and mechanical properties of high pressure die cast AM50 magnesium alloy. *Trans. Nonferrous Met. Soc. China* **23**, 66 (2013).
32. W. Zhou, Q. Li, H.J. Kang, and Q. Zhang: Microstructure and mechanical properties of AZ81 alloy with Gd. *Appl. Mech. Mater.* **117**, 1125 (2012).
33. Q. Guo, Z. Liu, P. Mao, and J. Sun: Effect of aging temperature on microstructure and mechanical properties of AZ81–4%Gd magnesium alloy. *Mater. Sci. Forum* **747**, 301 (2013).
34. Y. Miao, L. Yaohui, L. Jiaan, and S. Yulai: Corrosion and mechanical properties of AM50 magnesium alloy after being modified by 1 wt% rare earth element gadolinium. *J. Rare Earths* **32**, 558 (2014).
35. G.L. Song, A.L. Bowles, and D.H. St John: Corrosion resistance of aged die cast magnesium alloy AZ91D. *Mater. Sci. Eng., A* **366**, 74 (2004).
36. Y. Jiao, J. Zhang, L. He, M. Zhang, F. Jiang, W. Wang, L. Han, L. Xu, and R. Wu: Al–RE intermetallic phase stability and effects on corrosion behavior in cold-chamber HPDC AE44 alloy. *Adv. Eng. Mater.* **18**, 148 (2016).
37. Y.L. Song, Y.H. Liu, S.H. Wang, S.R. Yu, and X.Y. Zhu: Effect of cerium addition on microstructure and corrosion resistance of die cast AZ91 magnesium alloy. *Mater. Corros.* **58**, 189 (2007).
38. P. Xiaodong, L. Junchen, L. Wenjuan, Y. Yan, and W. Qunyi: Effect of Y on microstructure and mechanical properties as well as corrosion resistance of Mg–9Li–3Al alloy. *Rare Met. Mater. Eng.* **42**, 1993 (2013).
39. M. Nouri, X. Sun, and D.Y. Li: Beneficial effects of yttrium on the performance of Mg–3%Al alloy during wear, corrosion and corrosive wear. *Tribol. Int.* **67**, 154 (2013).
40. A. Srinivasan, S. Ningshen, U. Kamachi Mudali, U.T.S. Pillai, and B.C. Pai: Influence of Si and Sb additions on the corrosion behavior of AZ91 magnesium alloy. *Intermetallics* **15**, 1511 (2007).
41. D. Huang, J. Hu, G.L. Song, and X. Guo: Inhibition effect of inorganic and organic inhibitors on the corrosion of Mg–10Gd–3Y–0.5Zr alloy in an ethylene glycol solution at ambient and elevated temperatures. *Electrochim. Acta* **56**, 10166 (2011).
42. F. Rosalbino, E. Angelini, S. De Negri, A. Saccone, and S. Delfino: Electrochemical behaviour assessment of novel Mg-rich Mg–Al–RE alloys (RE = Ce, Er). *Intermetallics* **14**, 1487 (2006).
43. R. Arrabal, E. Matykina, A. Pardo, M.C. Merino, K. Paucar, M. Mohedano, and P. Casajus: Corrosion behaviour of AZ91D and AM50 magnesium alloys with Nd and Gd additions in humid environments. *Corros. Sci.* **55**, 351 (2012).
44. A.A. Moosa: Effect of lanthanum addition on the microstructure of Mg–4Al alloy. *Al-Khwarizmi Eng. J.* **7**, 75 (2011).
45. A. Zafari, H.M. Ghasemi, and R. Mahmudi: An investigation on the tribological behavior of AZ91 and AZ91 + 3 wt% RE magnesium alloys at elevated temperatures. *Mater. Des.* **54**, 544 (2014).
46. A. Zafari, H.M. Ghasemi, and R. Mahmudi: Tribological behavior of AZ91D magnesium alloy at elevated temperatures. *Wear* **292**, 33 (2012).
47. C. Taltavull, B. Torres, A.J. Lopez, and J. Rams: Dry sliding wear behavior of AM60B magnesium alloy. *Wear* **301**, 615 (2013).